SAND2022-7197C

Demonstration of Internal Digital Image Correlation for Fluid-Structure Interaction Measurements in a Hypersonic Wind Tunnel

Anshuman Pandey*, Bryan E. Schmidt†, Kyle P. Lynch‡, Katya M. Casper§, Steven J. Beresh¶, Rajkumar Bhakta ‖, Charley Downing **, Marie E. DeZetter ††, Russell Spillers ‡‡

This study demonstrates three-dimensional deformation measurements of a thin panel in hypersonic flow using internal miniature cameras. The panel was incorporated as the front face of a ramp that was placed at the aft end of a slender cone-slice geometry. The internal face of this panel was speckled and imaged using two on-board cameras. A Laser Doppler Vibrometer (LDV) provided simultaneous point measurements on the panel exterior. Panel images were processed using a commercial correlation-based DIC software and a custom wavelet-based optical flow analysis (wOFA) algorithm to extract the out-of-plane panel displacements. The technique was able to capture the static deformation of the panel while the LDV resolved the dynamic panel response due to the unsteady fluid loading.

I. Introduction

High temperature applications of thin materials such as in the extreme environments encountered by a hypersonic vehicle pose unique multi-physics problems [1]. A thin panel subjected to intense pressure and thermal loads has different vibration characteristics than in the case where no thermal loads are present [2]. This coupling of the thermal, fluidic and vibrational aspects of the problem, known as fluid-thermal-structure interaction (FTSI), make the design of hypersonic vehicles particularly challenging. The development of numerical tools used in the design process includes wind-tunnel measurements to provide physical understanding as well as for generation of validation datasets. As such, in addition to thermal and fluid information, it is important to obtain accurate full-field deformation measurements [3, 4]. This study demonstrates a technique using internal optical elements and a wavelet-based optical flow analysis (wOFA) to provide such spatially-resolved measurements of deformation.

Conventional methods of obtaining vibration include strain gauges, capacitance-based displacement sensors and

*Postdoctoral Appointee, Sandia National Laboratories, NM, Member AIAA
†Assistant Professor, Case Western Reserve University, OH, Senior Member AIAA
‡Senior Member of the Technical Staff, Sandia National Laboratories, NM, Senior Member AIAA
§Principal Member of the Technical Staff, Sandia National Laboratories, NM, Associate Fellow AIAA
¶Distinguished Member of the Technical Staff, Sandia National Laboratories, NM, Associate Fellow AIAA
‖Senior Test Operations Engineer, Sandia National Laboratories, NM
**Principal Technologist, Sandia National Laboratories, NM
††Technologist, Sandia National Laboratories, NM
‡‡Principal Technologist, Sandia National Laboratories, NM

piezoelectric accelerometers. These sensors are accurate and can be used in situations where the vibrations are small [5]. However, the mounting of sensors can produce slight changes in the vibrational characteristics of the object and the bandwidth of such sensors are limited by their design-specific internal resonance. Most importantly, these sensors are spatially averaged point measurements which result in low spatial resolution and preclude analysis of higher-order spatially-distributed structural modes. Many of these limitations can be overcome by an optical technique that uses pattern tracking to track movements of artificially induced spatial patterns on a structure [6]. Predominant among these are photogrammetry [7, 8] and digital image correlation (DIC) [9, 10] that use correlation algorithms to track high contrast dot grid pattern or random speckles, respectively, across deformed and reference images to obtain static deformation. The measurement resolution is very high; limited only by the resolution of the camera and the correlation window size of the algorithm used. Two synchronized cameras in a stereo configuration can provide out-of-plane deformations and use of high-speed cameras enable dynamic measurements that can also track phases of the structural modes [11].

A typical DIC/photogrammetry wind-tunnel experiment employs externally-mounted light-source and cameras to illuminate and capture the reflected light off a speckled deforming panel. For a high-speed tunnel, the density gradients produced due to impinging shocks and wall shear layers create variations in the index of refraction that subjects the reflected light to beam-steering effects. This causes apparent movement of speckles that has been exploited in the recent years as the basis for the background-oriented schlieren technique[12]. However for deformation measurements, it becomes a source of error since this speckle motion is not related to the movement of the panel [13–15]. For example, Lynch et al. [14] observed up to 30 μm false displacements in a shock tube during passage of a Mach 1.3 shock and Brouwer et al. [16] observed measurable distortions in their DIC measurement due to the presence of impinging shocks at Mach 2. Stronger shocks present in hypersonic testing are expected to produce larger distortions. In study of shock-induced FTSI, the source of error is also the predominant source of unsteady deformations and as such it is not possible to spectrally filter the distortions. Jones and Reu [13] conducted a systematic study on DIC images distorted by heat waves and noted that filtering methods only provide marginal reduction in errors and the best strategy, if possible, is to eliminate or mitigate this source of error. One approach of eliminating distortion effects in shock-induced FTSI studies is to conduct experiments on an external tunnel wall such that the structure can be imaged from the no-flow side [3, 17]. However this is not possible for typical model geometries that are placed in the center of the test section. Another approach is to use x-ray based DIC [18, 19] since, as compared to visible light, x-rays have higher energy that results in considerably less refraction effects in gases. However, the experimental setup for x-ray DIC is complicated and requires specialized equipment and speckling techniques.

In this work, a low-cost alternative: **internal-DIC** is demonstrated where miniature cameras and light-source are placed inside the wind-tunnel model. The non-canonical geometry shown in Fig. 1 has been used in the recent years at Sandia as a test-bed to understand three-dimensional shock-wave/boundary-layer interaction (SBLI) in flight-realistic

bodies [20, 21]. Use of a thin panel as the front face of the ramp along with long run duration of the Sandia Hypersonic Wind Tunnel (HWT) allow coupling of thermal, fluidic and structural aspects and enable controlled FTSI studies on this geometry [5]. However, the slenderness (7° half-angle cone) imposes severe restrictions on the space available to house the optical elements inside the cone. This necessitated the use of a mirror to fold the setup and two bare-bones board-cameras for stereo-imaging. This technique successfully captured the panel deformations and use of a concurrent time-resolved Laser Doppler Vibrometer (LDV) signal allowed tracking the dominant panel mode frequencies. Apart from the wind-tunnel tests, internal-DIC may be used in other applications where a conventional DIC setup would be too cost-, space- or bandwidth-intensive.

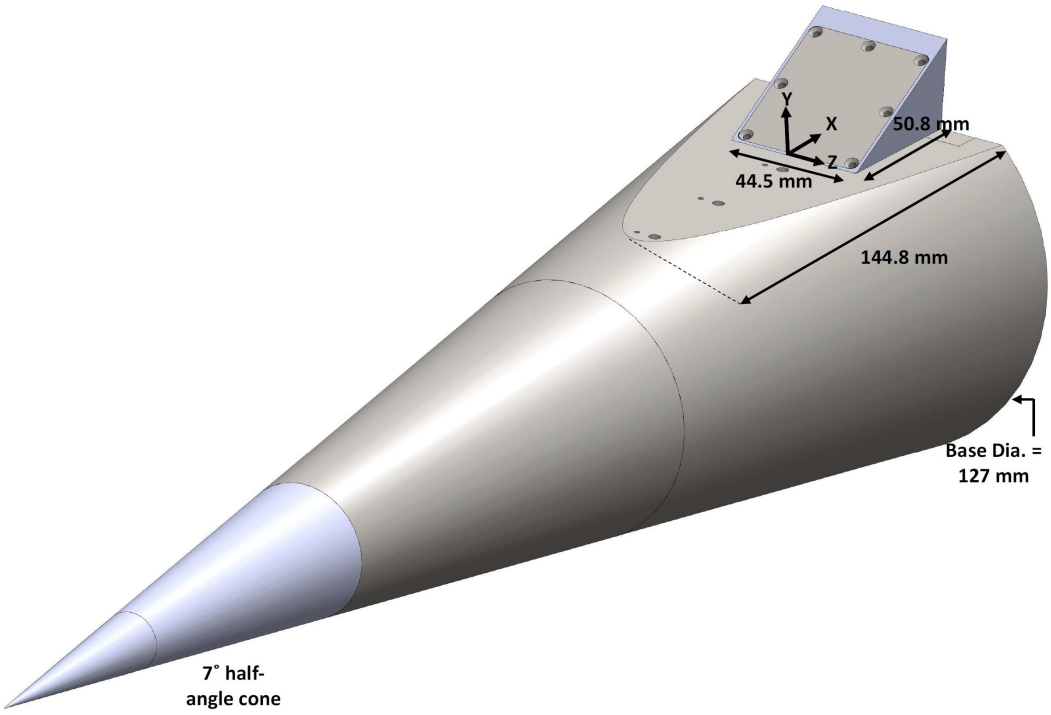

Fig. 1 Schematic of the model used in this work and the coordinate system rooted at mid-span of the slice-ramp corner

In addition to the optical setup, speckling pattern and tracking algorithm are an important consideration in a DIC experiment. In this work, along with the correlational algorithms used in conventional DIC, wOFA is proposed to track the speckled pattern. wOFA has a significant advantage compared to conventional DIC algorithms in terms of spatial resolution, because optical flow methods return the so-called "dense" estimations of the displacement field, i.e. one displacement vector per pixel in the input images. Therefore, there is minimal loss in spatial resolution when calculating displacements. wOFA is likely more accurate than DIC in the absolute sense as well, indicated by previous success in applying similar wavelet-based optical flow methods to particle image data in fluid flows (compared to PIV) [22–24] and for computing background-oriented schlieren images [25]. Optical flow methods have been applied successfully to

compute solid deformation in the literature by Xiao et al. [26]. In this work, the panel images have been analyzed using a wOFA algorithm to showcase its applicability in deformation measurements for the first time. The study demonstrates the feasibility of internal-DIC and wOFA for deformation measurements in high-speed wind tunnels.

II. Experimental Setup

A. Sandia Hypersonic Wind Tunnel and Test Conditions

The Sandia Hypersonic Wind Tunnel (HWT) is a conventional blowdown-to-vacuum facility with an interchangeable system of nozzles and heater sections for the selection of a desired Mach number in the test section. In this work, the Mach 8 system was used that has a 355.6 mm diameter axisymmetric test section. The tunnel employs a bottle farm that stores nitrogen (working fluid) at 689 MPa. A control valve between the high-pressure storage and the tunnel allows a P_0 range of 1720-6890 kPa and an in-line heater provides a T_0 range of 500-890 K. This provides a Reynolds number range from 3.3-20 x 10^6/m with a noise level of $3-5\%$, quantified as the RMS Pitot pressure between 0 to 50 kHz over the mean Pitot pressure [27]. Data presented in this work corresponds to two Re cases, 4.5 x 10^6/m and 16.2 x 10^6/m that result in a laminar and a turbulent inflow, respectively, in the SBLI region.

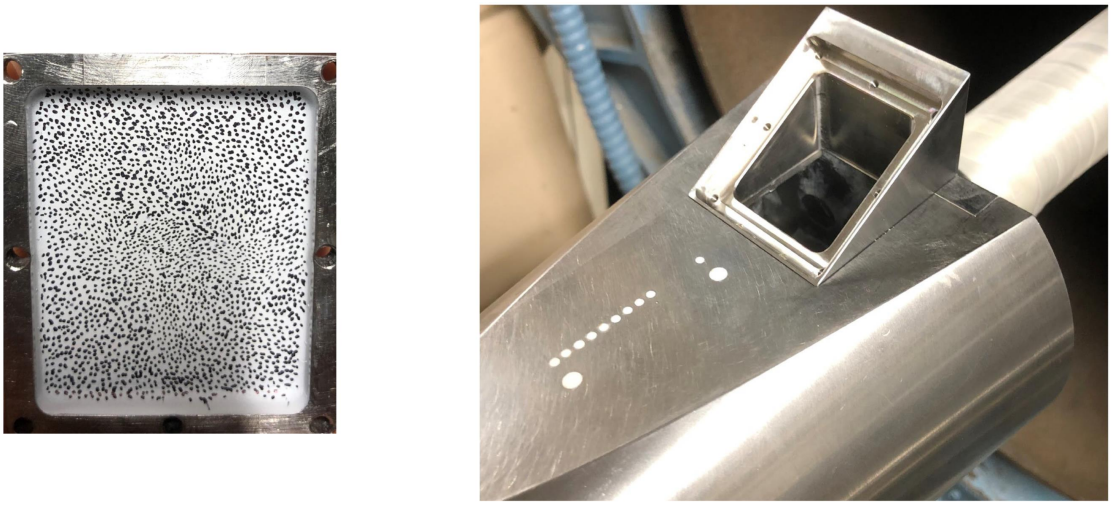

Fig. 2 Left: Speckle on the back-side of the panel. Right: Ramp frame and cone mounted in the HWT

B. Model and Sensors

The test model is a 7° half-angle slender cone with a base diameter of 0.127 m. Fig. 1 shows a schematic of this model. The cone has an axial cut that creates a 144.78 mm long hyperbolic slice. At its aft-end, a 50.8 mm long and 44.45 mm wide 30° hollow-ramp is placed. The model origin is located at the slice-ramp corner and at mid-span of the ramp (shown in Fig. 1). A 41.4 mm long and 34.2 mm wide thin stainless steel panel (0.5 mm thick) was mounted on the hollow-ramp frame to form its front face (see Fig. 2). This panel was subjected to the fluid-thermal loading of the

SBLI occurring on this geometry. A coordinate system (x', y') rooted at the centroid of this panel was used to discuss the deformation data. The x' and y' panel displacements are denoted by U and V, respectively, and W denotes the out-of-plane displacement. RTV was used between the panel and the frame as a sealant and the panel was mounted on to the frame using seven bolts, tightened to 0.565 N-m torque each, in order to obtain clamped boundary conditions around the panel. Plaster and subsequent polishing over the hole cavities ensured that the wedge face was free of any surface discontinuities. Breathing holes in the base plate allowed the inside of the cone and the wedge cavity to equilibrate with the base pressure aft of the cone. The model was mounted using a sting at the base of the cone and all testing was done at zero angle of attack.

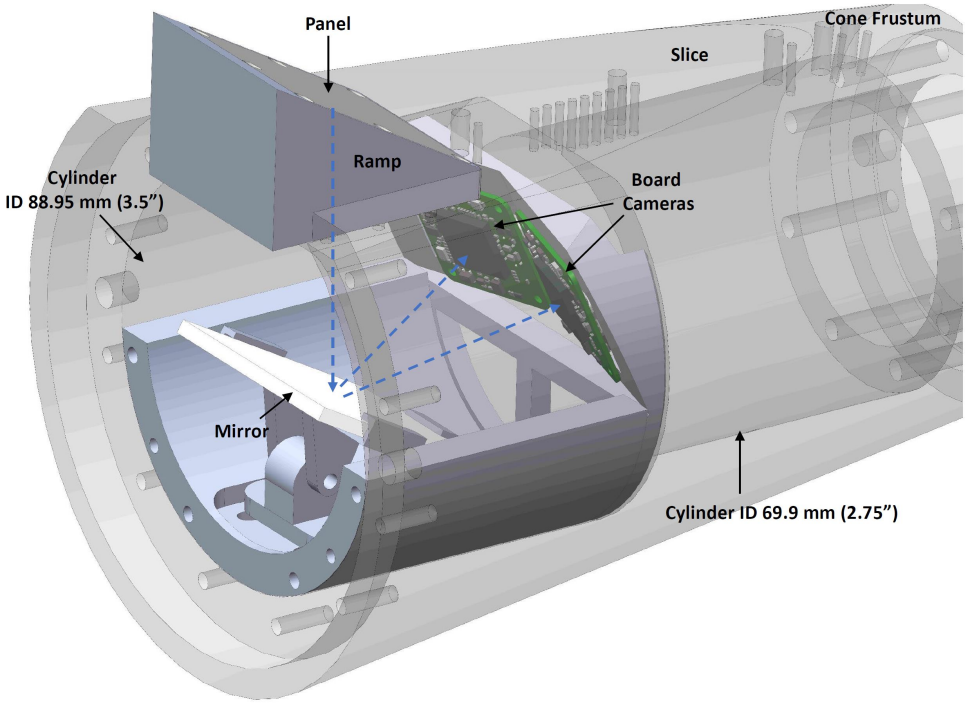

Fig. 3 Schematic of the internal-DIC components inside the cone

To speckle the back-side of the panel, first a few coats of a white primer paint (VHT SP101) was applied and then dots were randomly drawn using a black ultra-fine marker (Sharpie). These provided an approximate dot-size of 3-5 pixels in the final images as recommended by the DIC best-practices guide [28]. The resulting speckle-pattern can be seen in Fig. 2(a). This speckled panel was viewed through a mirror using two cameras that were mounted inside the cone as shown in the schematic in Fig. 3. The space inside the cone was composed of concentric cylinders that decreased in size from the base to the nose. The most downstream cylinder, which was nearest to the ramp, had an internal diameter of 88.95 mm and a length of 72.97 mm. This volume primarily limited the size of the setup while the significantly smaller upstream cylinder (inner diameter of 69.9 mm) was used for turning the cables back downstream that were routed through the base, sting, and then out of the wind tunnel. The internal assembly was mounted to the

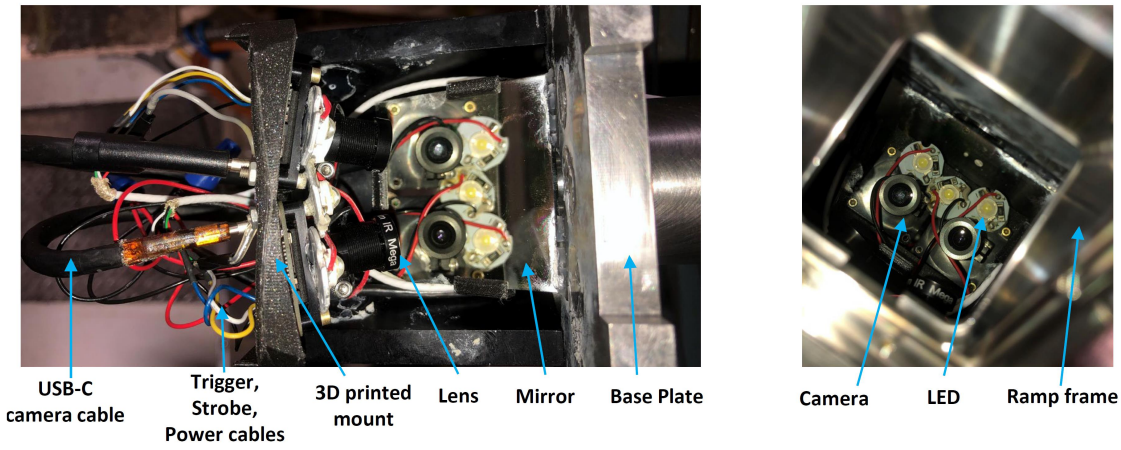

Fig. 4 Left: Photo of internal-DIC optics mounted in the HWT. Cone removed. Right: Cone in place, panel removed. Looking through the open ramp frame.

cone base plate using a metallic semi-cylinder shell. Once the base plate was sting-mounted in the HWT, the cone body could be independently removed to access the internal optical elements and make any changes prior to the run if necessary. A 50.8 mm square mirror (Thor Labs BBSQ2-E02) and two monochrome board cameras (Imaging Source DMM 37UX273-ML) were mounted to the semi-cylinder using in-house 3D printed parts (see Fig. 4). The stereo-angle was limited by the inner-cylinder volume and the magnification provided by the available lenses. A 6 mm M12 lens (IR Mega) optimized the field of view for the highest possible frame-rate of 400 Hz. Three white light emitting diodes (LED) were used to provide illumination of the speckled panel. These were also mounted on the 3D printed part around the cameras as seen in Fig. 4.

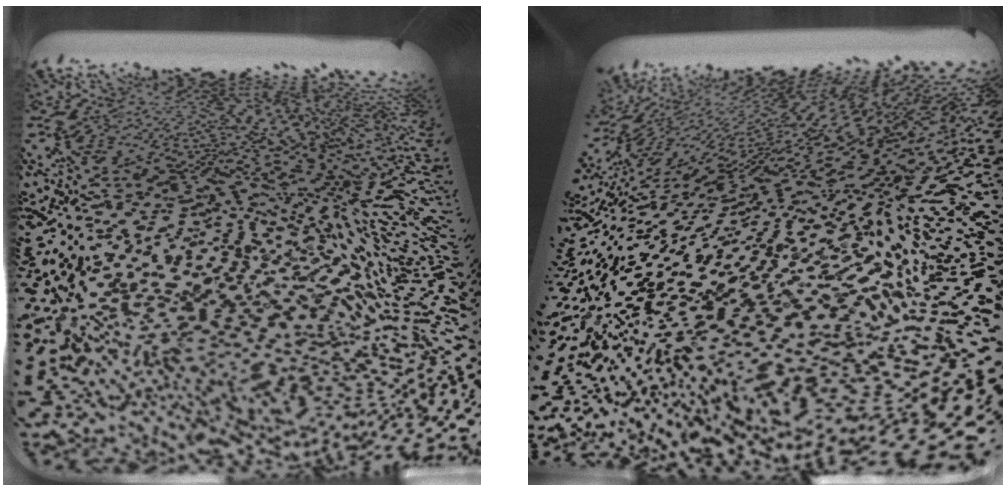

Fig. 5 Instantaneous images of the panel acquired during a run. Left: Camera 1, Right: Camera 2.

Cameras were triggered using an SRS box to ensure simultaneous acquisition by the two cameras and the strobe

signals were recorded for phase averaging. To capture the phases of the dominant natural modes which were a few kHz in frequency, the exposure time of the cameras needed to be small. However, a small exposure time necessitated the use of camera gain which also increased the imaging noise. More LEDs may be added in future studies to increase the illumination needed for short exposures [28]. Images were acquired with an exposure of 10 μs and a 25 dB gain was applied in the acquisition software. Instantaneous images acquired from the two cameras during a run are shown in Fig. 5. The resulting images had sufficient contrast for the DIC algorithms to be able to extract deformation. The cameras did not have an on-board memory and for best acquisition rate, high throughput USB-C cables and a computer with compatible USB 3.1 slots and large RAM were used. This allowed 740x720 pixel images to be acquired at 400 Hz for over 40 seconds of acquisition. The cameras and the LEDs do not have any cooling and to avoid overheating these were turned-on few seconds prior to the run. Camera calibration was performed by removing the speckled panel and waving a calibration target near the open frame face (see Fig. 2). A checkered target was printed on a sticker paper and pasted on a piece of acrylic for the Matlab based camera calibration used by wOFA. For the commercial software based processing, a 3 mm calibration target provided by Correlated Solutions was used. These calibration images were acquired several times during the test campaign.

C. Schlieren and LDV measurements

A concurrent schlieren visualization was carried out to observe the SBLI flow-field that generates the unsteady fluid loading on the panel. A high-speed laser (Cavilux Smart) that generated pulses of 10 ns duration at 200 kHz was used. The z-type schlieren configuration used two 450.8 mm diameter spherical mirrors for light-collimation and a knife edge oriented horizontally to resolve vertical gradients in density. The density gradients in the whole slice-ramp region was captured by a high-framerate camera (Phantom TMX7510) with a 1280 x 288 pixel area that provided a resolution of 7.67 pixels/mm.

A laser doppler vibrometer (LDV) was used to provide time-resolved vibration measurements at the center of the panel. The LDV system consists of a Polytec OFV-511 sensor head with a fiber optic cable and a mini-sensor that was mounted on top of the HWT as shown in Fig. 6. The laser beam was focused at the center of the panel to ensure good signal levels. The LDV signal was processed by a vibrometer controller (Polytec OFV-5000) using a velocity decoder (Polytec VD-02). Measurement range of 25 mm/s/V was selected with a low pass filter frequency of 1.5 MHz. Signal was also high pass filtered at 100 Hz to minimize noise due to tunnel vibrations. Acquisition of the LDV signal was carried out on the same time stamp as the strobe signal from the DIC cameras to allow phase resolving the images. A Labview controlled NI PXIe system with NI-6396 modules was used for acquiring these signals at 5 MHz.

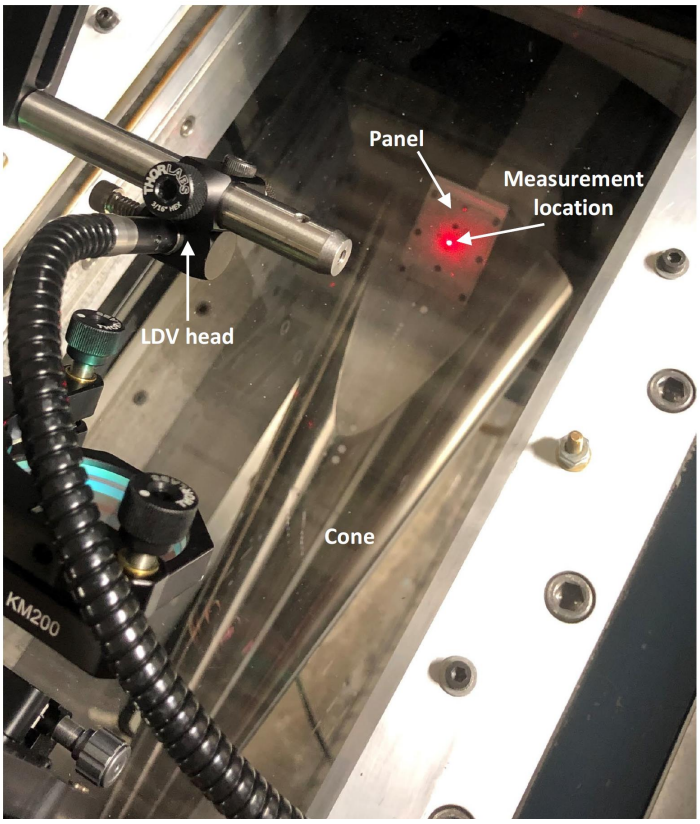

Fig. 6 LDV instrumentation with the model in HWT. Red dot on the panel is created by the LDV laser.

D. Commercial DIC software

A commercial DIC software (Correlated Solutions VIC-3D 9) was also used for processing the images acquired during the bench-top tests and the HWT tests. The software is based on correlational algorithms [9] that cross-correlate across windows of appropriate size to extract the motion of the speckle pattern. A window size of 31 pixels was used in the processing that resulted in a resolution of 2.3 pixels/mm. Camera calibration was performed using a hybrid approach in the VIC-3D software which uses both a calibrated dot-grid and the speckled panel. In this, the correlation results from the speckled panel are used to calibrate a 5th order variable-ray origin (VRO) camera model, while the dot-grid target provides the image scaling (pixel to mm).

E. Wavelet-based Optical Flow Analysis

The stereoscopic calibration for the virtual cameras is performed using standard methods from the literature implemented in MATLAB [29–31]. wOFA computes a two-dimensional displacement field between a pair of images as described below in this section, so additional steps are necessary to compute a three-dimensional displacement field from a stereoscopic image pair. Analysis proceeds as follows.

1) Match the left and right references images together using wOFA along with the known camera calibration

parameters to rectify the 3D reference scene.

2) Repeat Step 1 for the data (deformed) images to rectify the 3D data scene.
3) Use wOFA to match the left reference image to the left data image.
4) Using the known 3D position of the target in the reference and data scene and the displacement between the two left images from Step 3, compute the 3D displacement field.

The details regarding the two-dimensional wOFA method and implementation are described in detail in [**?**] for the computation of BOS images, and the interested reader is referred there for further information as the methodology is identical to the present application. Briefly, the displacement field $\vec{d}$ is estimated from a minimization problem given by

$$\hat{\vec{d}} = \underset{\vec{\psi}}{\operatorname{argmin}} \; J_D\left(I_0, I_1, \vec{\psi}\right) + \lambda J_R\left(\vec{\psi}\right). \tag{1}$$

In Eq. (1), $\vec{\psi}$ is the wavelet transform of the displacement $\vec{d}$; J_D is a penalty function, referred to as the data term, which penalizes mismatch between the input 2D images I_0 and I_1, where I_1 has been warped by $\vec{d}$; J_R is a regularization term that enforces smoothness on the displacement field; and λ is a scalar parameter that balances the two terms. As shown in Eq. (1), wOFA performs the minimization process on the wavelet transform of the velocity field rather than the velocity field itself, which distinguishes it from other optical flow methods in the literature, such as that of Xiao et al. [26]. Using the truncated wavelet basis provides closure to the ill-posed inverse problem in Eq. (1) and dramatically increases computational efficiency with effectively no loss in fidelity.

The data term, J_D, is based on the displaced frame difference (DFD) equation, given by

$$I_0\vec{x} - I_1\vec{x} + \vec{d}\vec{x} = 0, \tag{2}$$

which simply states that the intensity I at a given position $\vec{x}$ is conserved, and only changes at position $\vec{x}$ as a result of deformation of the target. The image intensity is normalized to account for changes in illumination prior to computation of the displacement field.

III. Results

A. Flow-field description

The flowfield organization is strongly dependent on the Re of the test since the boundary layer state governs the extent of the SBLI region. Fig. 7 shows a temporally averaged schlieren image for both the cases discussed here. At lower Re of 4.5 x 10^6/m, the boundary layer developing on the cone is laminar which is highly susceptible to separation. As such, separation occurs just downstream of the cone-slice corner with a separation bubble extending over the whole slice region. The shear layer, visible as a light-colored diffuse section in Fig. 7 (top), reattaches slightly downstream of

the middle of the panel (shown as a red line). Contrary to this, the turbulent boundary layer in the high Re case has a much smaller separation region (separating at x ≈ -20). Fig. 7 (bottom) shows a considerably thickened boundary layer downstream of the cone-slice corner and a small separation bubble near the slice-ramp corner. The reattachment location is further upstream of the reattachment in the laminar case with the reattachment shock emanating at approximately the center of the panel. Further details on the Re dependence of the flowfield can be found in [20].

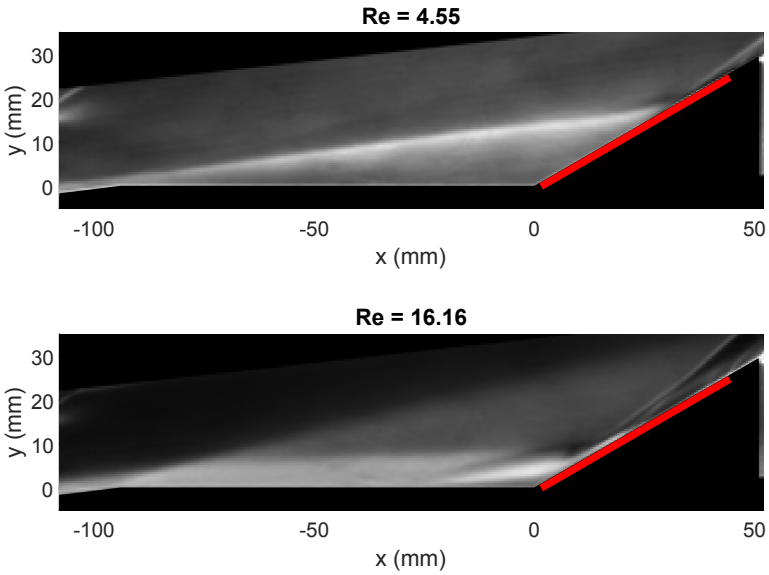

Fig. 7 Ensemble averaged schlieren image. Top: Re = 4.5 x 10^6/m, bottom: 16.2 x 10^6/m. Red line indicates the extent of the panel.

The flow unsteadiness in the two cases can be explored by computing spectral proper orthogonal decomposition (SPOD) of the schlieren data acquired at 200 kHz. Fig. 8 shows the energy distribution of the first three SPOD modes. Good separation in the energy content between the first and the higher order modes indicates presence of coherent flow phenomena [32] and frequency peaks indicate increased energy at a particular frequency. Such a flow phenomena can induce structural vibrations in the panel in addition to its natural modes excited by broadband disturbances. Instabilities in the laminar case lead to a few such broad frequency peaks one of which is related to the shear layer flapping occurring at 16.6 kHz (marked in Fig. 8(left)). In comparison, the turbulent case has broadband distribution of energy as shown in Fig. 8(right). Further discussion of instabilities in the laminar case can be found in [21].

B. LDV data

Panel response in the flow was measured using a laser doppler vibrometer (LDV) mounted externally (see Fig. 6). This temporally-resolved point measurement was obtained at the center of the panel and captures its dominant modes of vibration. Power spectral density was computed on a 10 second segment of the raw LDV data (in voltage) with a frequency resolution of 200 Hz. These results for the two cases are shown in Fig. 9 in the normalized sense where

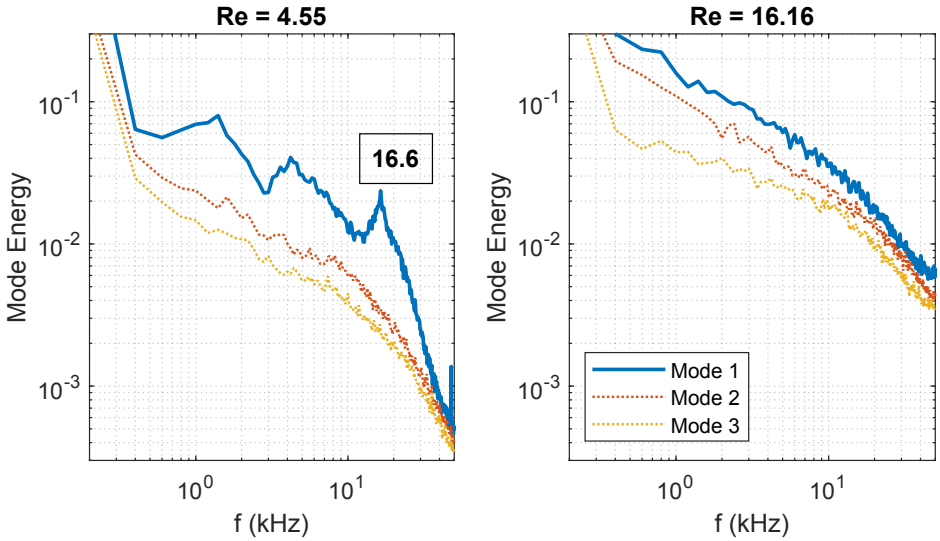

Fig. 8 SPOD mode energy for left: Re = 4.5 x 10^6/m and right: Re = 16.2 x 10^6/m.

the normalization was carried out using the edge dynamic pressure after the cone nose shock. This normalization corrects for the increased baseline energy available in the flow at higher Re. The two cases show peaks at mostly similar frequencies suggesting that these are due to the natural modes of the panel. Slight variations in the peak frequencies could be related to the differences in temperatures and pressure across the panel for the two Re cases. Higher frequency peaks are stronger for the turbulent case due to the availability of broadband forcing as compared to the laminar case which lacks in energy at the high frequencies. A couple of peaks in the laminar regime, at 6.4 kHz and 16.6 kHz, stand out and have been marked in Fig. 9 (bottom). These are presumably related to the increased forcing generated by the instabilities in the flow. The 16.6 kHz vibration is likely related to the shear layer flapping phenomena discussed above; this was also observed in a previous study [5] using a thicker (1 mm) panel and accelerometers as vibration sensors. The 6.4 kHz peak may be related to the broad peak in the 3-7 kHz range in Fig. 9(left) or could be related to a flow phenomena not captured by the spanwise integrated schlieren. Further details on the differences between the pressure fluctuations in the two cases can be found in [21].

C. Internal-DIC data

The stereo-image pairs taken using the on-board cameras were processed using a commercial DIC code to obtain the three dimensional deformations. A one second segment was acquired prior to the run after the tunnel pressure had been reduced to near vacuum. The averaged result is shown in Fig. 10; the three components of the displacement data show near zero values as expected. All displacements shown in this paper are in mm. During the run, the pressure difference across the panel creates a large deformation at the center of the panel as shown in the averaged deformation data in Fig.

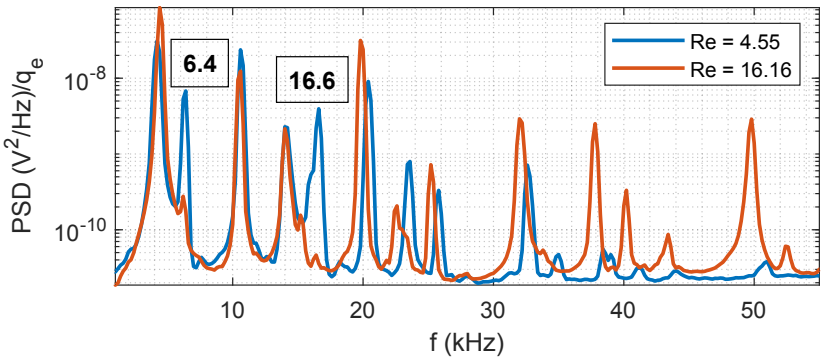

Fig. 9 Normalized power spectral density of LDV data for the two Re cases.

11 (right). This average deformation was obtained by averaging 4000 instantaneous deformation fields acquired over 10 seconds for the high Re case. This large bulge, of the order of 300 μm, is inwards towards the cameras (or away from the flow). Conservation of mass enforces in-plane deformations (U and V) that are spatially distributed and are of the order of 10-50 μm. The resolution of these figures is determined by the resolution of the acquired images and the subset window size used for correlation. The resulting images produced a 82x96 pixel deformation field as shown.

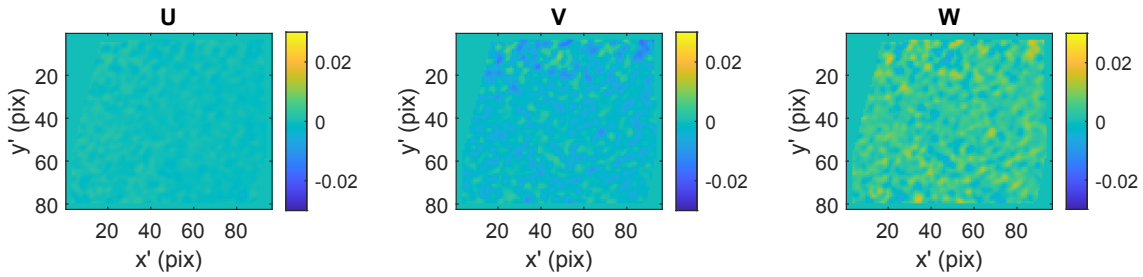

Fig. 10 Average displacement pre-run

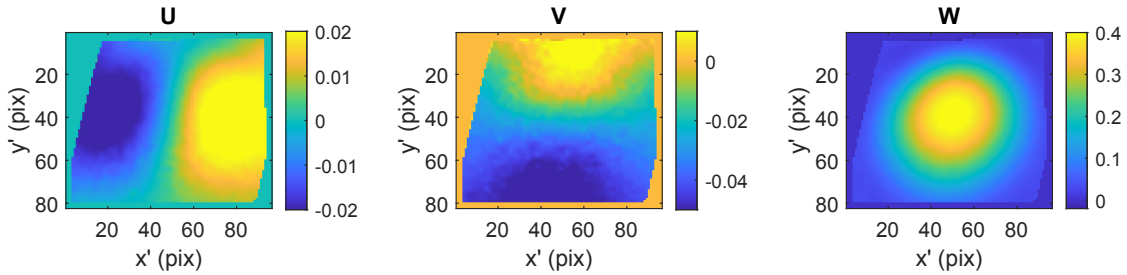

Fig. 11 Average displacement during run. Re = 16.2 x 10^6/m

The low Re case is shown in Fig. 12 where a longer wind-tunnel acquisition time of 40 seconds was used. The temporally averaged deformation (over 16,000 images) demonstrates qualitatively similar deformations as the high Re case, however, the size and position of the bulge is markedly different. A comparison between the two cases is shown

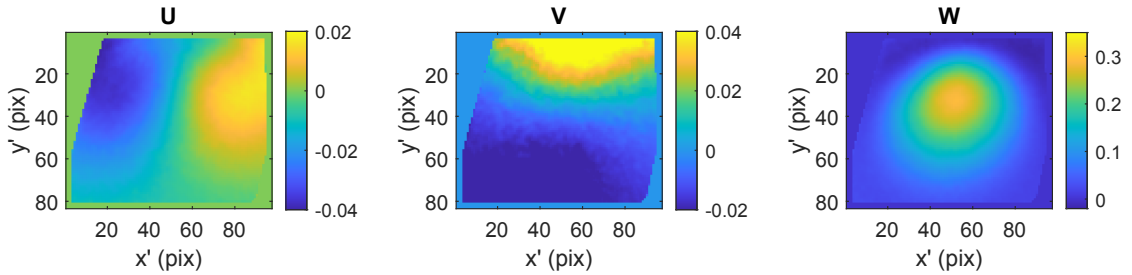

Fig. 12 Average displacement during run. Re = 4.55 x 10^6/m

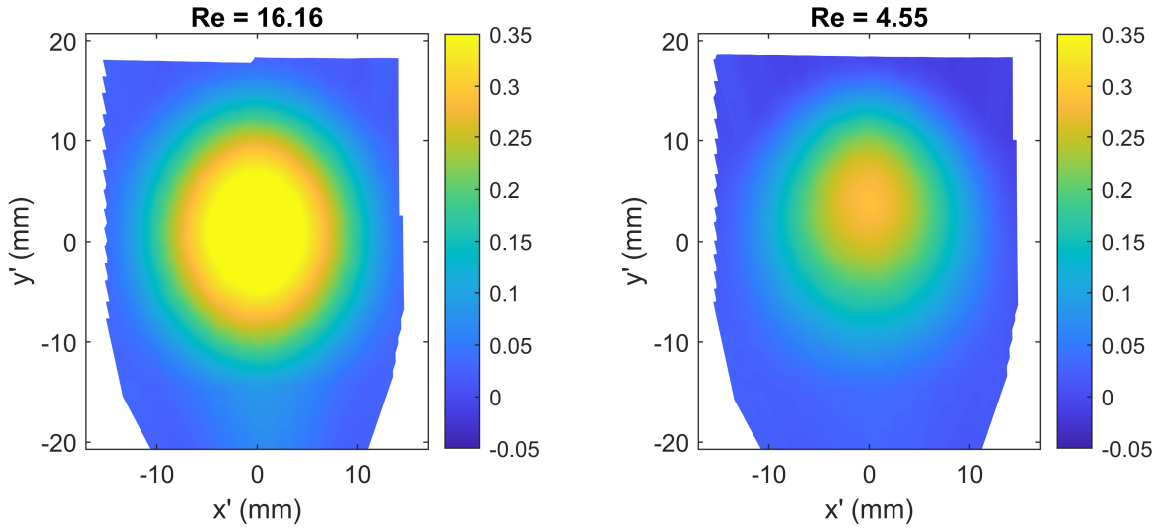

Fig. 13 Average out-of-plane displacement in physical coordinates.

in physical coordinates (along the panel dimensions) in Fig. 13. The low Re out-of-plane deformation is less (of the order of 200 μm) than the high Re case due to reduced pressure differential across the panel. In addition, the bulge is located further downstream along the panel suggesting the effect of a more downstream reattachment and shear layer impingement in this case (see Fig. 7). These reinforce the LDV results that show the panel deformation is directly related to the unsteady pressure and thermal loading of the flowfield.

The results from the wOFA algorithm are shown in Fig. 14 in physical coordinates. Mappping artifacts are observed near the bottom corner and top part of the data. Apart from these, the deformation values correspond well with the values obtained using correlation-based software as shown in Fig. 13. A dominant benefit of wOFA is the high spatial resolution of the output results; here wOFA provided deformation fields in the acquired image resolution of 600x700 pixels as compared to only 82x96 pixels obtained from window-based correlations. Overall, the qualitative and quantitative agreement between the datasets suggests promise in using wOFA for deformation analysis.

The minitaure cameras used in this work were limited to acquisition rates of 400 Hz. However, the natural modes of

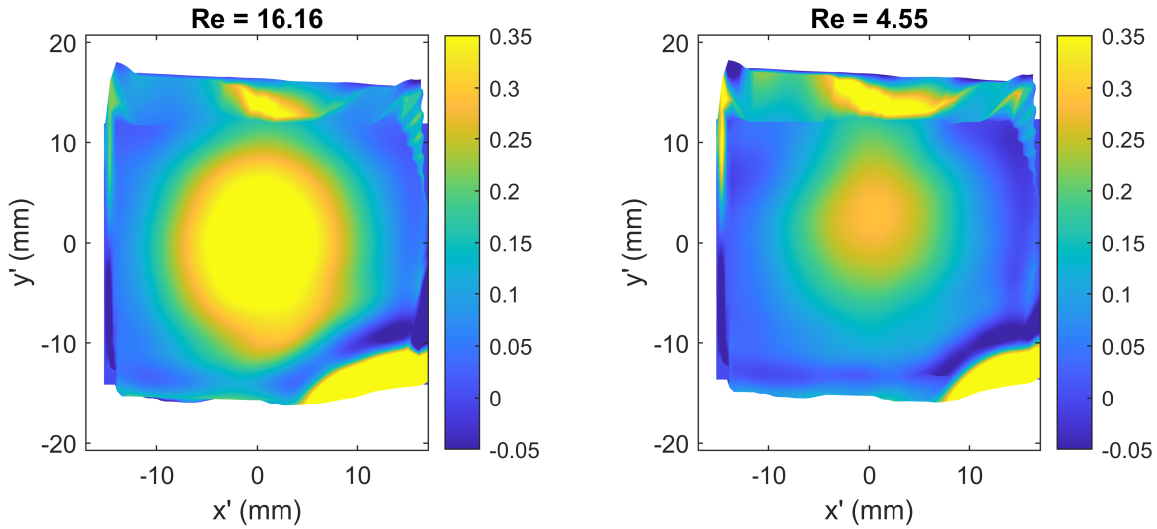

Fig. 14 Average out-of-plane displacement obtained from wOFA.

the panel have frequencies in the kHz range as shown in Fig. 9. To obtain panel deformations due such high frequency modes, phase averaging is needed. Though phase averaging using the LDV signal has not been presented in this work, a proper orthogonal decomposition (POD) based conditional average is presented below. The deformation images resulting from the correlation-software have been used for the lower Re case. POD was conducted on the out-of-plane component for the 16,000 images after detrending the long term variation using a 20 Hz high pass filter. This resulted in a reduced order representation of the motion of the panel during the run. The dominant POD modes best-represent the deformation data in the least-square sense and the temporal coefficients of each POD mode represents its contribution in the images.

The spatial mode of the 2nd POD mode is shown in Fig. 15 along with its temporal coefficient in the data set. This mode is similar to a (2,1) natural mode of a rectangular panel with two anti-symmetric lobes along the longer axis. The coefficients have a zero-mean (black-dashed line) and the extent of their variation are shown using the dashed red lines representing the standard deviation. Images with temporal coefficients higher and lower than the standard deviation were binned and averaged. Approximately 2500 images were found in each bin with the remaining 11,000 images being not used. This conditional average resulted in images with stronger contribution of the opposing phases of the POD mode shown in Fig. 15. These averages and their difference are shown in Fig. 16. The conditional averages are dominated by the actual shape of the panel which is similar for both the bins and is similar to the result shown in Fig. 12. Difference between the two bins, does however highlight the effect of the spatial pattern generated by this spatial mode. In future work, the LDV signal will be used to understand if the images in the two bins do actually demonstrate phase differences so that a connection between the shown POD spatial mode and the (2,1) panel natural mode can be made.

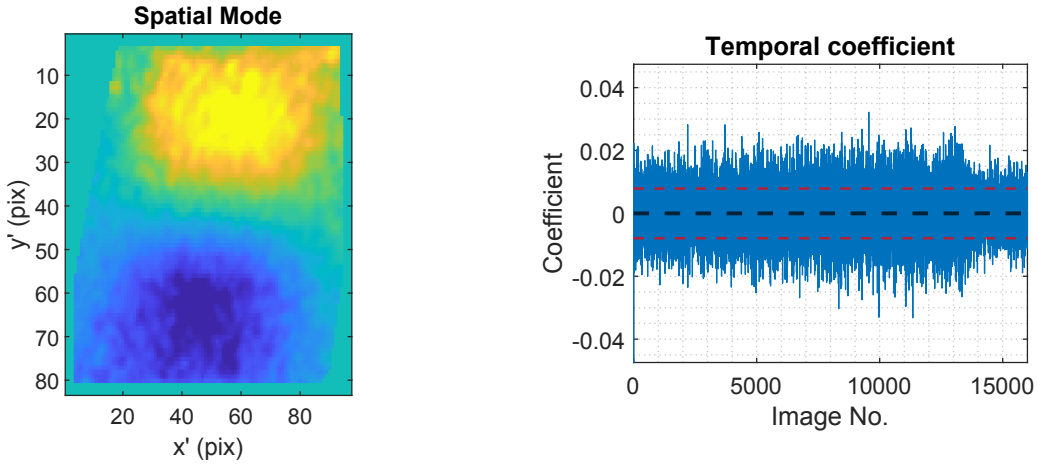

Fig. 15 POD mode 2 for Re = 4.55 x 10^6/m. Left: Mode shape, Right: Temporal coefficient.

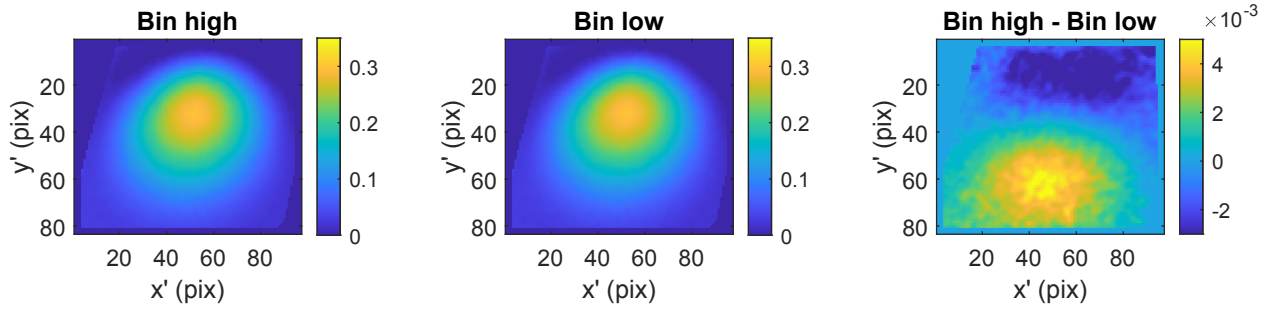

Fig. 16 Conditional averaging based on POD temporal coefficients. Left: Bin with High values, Center: Bin with Low values, Right: Difference between the two bins. Re = 4.55 x 10^6/m

IV. Conclusion

This study demonstrated the feasibility of using miniature cameras inside a hypersonic wind tunnel model to measure structural deformations arising due to fluid and thermal effects. In addition, the feasibility of a wavelet-based optical flow analysis (wOFA) algorithm for extracting three-dimensional deformation from images of a speckled structure was also demonstrated. These experiments were carried out on a thin panel incorporated on a slender cone-slice-ramp geometry that was tested under laminar and turbulent conditions. The panel deformed under fluid and thermal loading and this deformation was captured by the combined internal-DIC and wOFA framework. Quasi-steady deformations due to pressure differential was higher in the high Re case where the out-of-plane deformation bulge was centered in the panel. For the low Re case, a further downstream reattachment resulted in bulge that was offset downstream of the center. High frequency unsteady displacements at the center of the panel were captured by LDV. These showed that the panel is driven by the unsteady shear layer instabilities and boundary layer turbulence. At this time, the internal-DIC framework was limited by the low frame rate of the miniature cameras that could not resolve the panel modes. Future

processing will look to use the LDV signal to resolve the phases of the DIC images and average them. Furthermore, mapping errors in the wOFA analysis will be corrected to improve its accuracy.

V. Acknowledgments

Thomas Grasser designed the wind-tunnel model and David Autenrieth procured the thin panel used in this work. Elizabeth Jones provided guidance on the DIC analysis. Sandia National Laboratories is a multi-mission laboratory managed and operated by National Technology and Engineering Solutions of Sandia, LLC., a wholly owned subsidiary of Honeywell International, Inc., for the U.S. Department of Energy's National Nuclear Security Administration under contract DE-NA0003525. The views expressed in the article do not necessarily represent the views of the U.S. Department of Energy or the United States Government.

References

[1] McNamara, J. J., and Friedmann, P. P., "Aeroelastic and aerothermoelastic analysis in hypersonic flow: Past, present, and future," 2011, pp. 1089–1122. doi:10.2514/1.J050882.

[2] Freydin, M., Levin, D., Dowell, E. H., Varigonda, S. V., and Narayanaswamy, V., "Natural frequencies of a heated plate: Theory and experiment," *AIAA Journal*, Vol. 58, 2020, pp. 4969–4973. doi:10.2514/1.J059660.

[3] Spottswood, S. M., Smarslok, B. P., Perez, R. A., Beberniss, T. J., Hagen, B. J., Riley, Z. B., Brouwer, K. R., and Ehrhardt, D. A., "Supersonic Aerothermoelastic Experiments of Aerospace Structures," *AIAA Journal*, Vol. 59, 2021, pp. 5029–5048. doi:10.2514/1.J060403.

[4] Daub, D., Willems, S., and Gülhan, A., "Experiments on aerothermoelastic fluid–structure interaction in hypersonic flow," *Journal of Sound and Vibration*, 2022. doi:10.1016/j.jsv.2021.116714.

[5] Pandey, A., Casper, K. M., Soehnel, M., Spillers, R. W., Bhakta, R., and Beresh, S. J., "Hypersonic Fluid-Structure Interaction on the Control Surface of a Slender Cone," 2021. doi::10.2514/6.2021-0909.

[6] Helfrick, M. N., Niezrecki, C., Avitabile, P., and Schmidt, T., "3D digital image correlation methods for full-field vibration measurement," *Mechanical Systems and Signal Processing*, Vol. 25, 2011, pp. 917–927. doi:10.1016/j.ymssp.2010.08.013.

[7] Gramola, M., Bruce, P. J. K., and Santer, M., "Photogrammetry for accurate model deformation measurement in a supersonic wind tunnel," *Experiments in Fluids*, Vol. 60, 2019. doi:10.1007/s00348-018-2652-7.

[8] Whalen, T. J., Schöneich, A. G., Laurence, S. J., Sullivan, B. T., Bodony, D. J., Freydin, M., Dowell, E. H., and Buck, G. M., "Hypersonic fluid–structure interactions in compression corner shock-wave/boundary-layer interaction," *AIAA Journal*, Vol. 58, 2020, pp. 4090–4105. doi:10.2514/1.J059152.

[9] Schreier, H., Orteu, J.-J., and Sutton, M. A., *Image Correlation for Shape, Motion and Deformation Measurements*, Springer US, 2009. doi:10.1007/978-0-387-78747-3.

[10] Pan, B., "Digital image correlation for surface deformation measurement: Historical developments, recent advances and future goals," *Measurement Science and Technology*, Vol. 29, 2018. doi:10.1088/1361-6501/aac55b.

[11] Beberniss, T. J., and Ehrhardt, D. A., "High-speed 3D digital image correlation vibration measurement: Recent advancements and noted limitations," *Mechanical Systems and Signal Processing*, Vol. 86, 2017, pp. 35–48. doi:10.1016/j.ymssp.2016.04.014.

[12] Richard, H., and Raffel, M., "Principle and applications of the background oriented schlieren (BOS) method," *Measurement Science and Technology*, Vol. 12, 2001, pp. 1576–1585. doi:10.1088/0957-0233/12/9/325.

[13] Jones, E., and Reu, P., "Distortion of Digital Image Correlation (DIC) Displacements and Strains from Heat Waves," *Experimental Mechanics*, Vol. 58, 2018, pp. 1133–1156. doi:10.1007/s11340-017-0354-3.

[14] Lynch, K. P., Jones, E. M. C., and Wagner, J. L., "High-Precision Digital Image Correlation for Investigation of Fluid-Structure Interactions in a Shock Tube," *Experimental Mechanics*, Vol. 60, 2020, pp. 1119–1133. doi:10.1007/s11340-020-00610-8.

[15] Beberniss, T. J., and Ehrhardt, D. A., "Visible Light Refraction Effects on High-Speed Stereo Digital Image Correlation Measurement of a Thin Panel in Mach 2 Flow," *Experimental Techniques*, Vol. 45, 2021, pp. 241–255. doi:10.1007/s40799-020-00408-2.

[16] Brouwer, K. R., Perez, R. A., Beberniss, T. J., Spottswood, S. M., and Ehrhardt, D. A., "Experiments on a Thin Panel Excited by Turbulent Flow and Shock/Boundary-Layer Interactions," *AIAA Journal*, Vol. 59, 2021, pp. 2737–2752. doi:10.2514/1.J060114.

[17] Eitner, M., Musta, M., Vanstone, L., Sirohi, J., and Clemens, N., "Modal Parameter Estimation of a Compliant Panel Using Phase-based Motion Magnification and Stereoscopic Digital Image Correlation," *Experimental Techniques*, Vol. 45, 2021, pp. 287–296. doi:10.1007/s40799-020-00393-6.

[18] Jones, E., Quintana, E., Reu, P., and Wagner, J., "X-Ray Stereo Digital Image Correlation," *Experimental Techniques*, Vol. 44, 2020, pp. 159–174. doi:10.1007/s40799-019-00339-7.

[19] James, J. W., Jones, E. M. C., Quintana, E. C., Lynch, K. P., Halls, B. R., and Wagner, J. L., "High-Speed X-Ray Stereo Digital Image Correlation in a Shock Tube," *Experimental Techniques*, 2021. doi:10.1007/s40799-021-00508-7.

[20] Pandey, A., Casper, K. M., Spillers, R. W., Soehnel, M., and Spitzer, S., "Hypersonic Shock Wave-Boundary-Layer Interaction on the Control Surface of a Slender Cone," 2020, p. 815. doi:10.2514/6.2020-0815.

[21] Pandey, A., Casper, K. M., Guildenbecher, D. R., Beresh, S. J., Bhakta, R., DeZetter, M. E., and Spillers, R., "Instability Measurements in Hypersonic Flow on a Three-Dimensional Cone-Slice-Ramp Geometry," American Institute of Aeronautics and Astronautics, 2022. doi:10.2514/6.2022-1578.

[22] Schmidt, B. E., and Sutton, J. A., "High-resolution velocimetry from tracer particle fields using a wavelet-based optical flow method," *Experiments in Fluids*, Vol. 60, 2019, p. 37. doi:10.1007/s00348-019-2685-6.

[23] Schmidt, B. E., and Sutton, J. A., "Improvements in the accuracy of wavelet-based optical flow velocimetry (wOFV) using an efficient and physically based implementation of velocity regularization," *Experiments in Fluids*, Vol. 61, 2020, p. 32. doi:10.1007/s00348-019-2869-0.

[24] Schmidt, B. E., and Sutton, J. A., "A physical interpretation of regularization for optical flow methods in fluids," *Experiments in Fluids*, Vol. 62, 2021, p. 34. doi:10.1007/s00348-021-03147-1.

[25] Schmidt, B. E., and Woike, M. R., "Wavelet-Based Optical Flow Analysis for Background-Oriented Schlieren Image Processing," *AIAA Journal*, 2021, pp. 1–8. doi:10.2514/1.J060218.

[26] Xiao, F., Zhao, R., and Sun, P., "Three-dimensional displacement measurement based on the combination of digital image correlation and optical flow," *Applied Optics*, Vol. 55, 2016, p. 8207. doi:10.1364/AO.55.008207.

[27] Casper, K. M., "Hypersonic Wind-Tunnel Measurements of Boundary-Layer Pressure Fluctuations," , 2009. URL `https://apps.dtic.mil/sti/citations/ADA504177`.

[28] Jones, E. M. C., and Iadicola, M., "A Good Practices Guide for Digital Image Correlation," , 10 2018. doi:10.32720/idics/gpg.ed1.

[29] Heikkila, J., and Silven, O., "A four-step camera calibration procedure with implicit image correction," IEEE Comput. Soc, 1997, pp. 1106–1112. doi:10.1109/CVPR.1997.609468.

[30] Zhang, Z., "A flexible new technique for camera calibration," *IEEE Transactions on Pattern Analysis and Machine Intelligence*, Vol. 22, 2000, pp. 1330–1334. doi:10.1109/34.888718.

[31] Kaehler, A., and Bradski, G., *Learning OpenCV 3: Computer Vision in C++ with the OpenCV Library*, O'Reilly UK Ltd., 2017.

[32] Towne, A., Schmidt, O. T., and Colonius, T., "Spectral proper orthogonal decomposition and its relationship to dynamic mode decomposition and resolvent analysis," *Journal of Fluid Mechanics*, Vol. 847, 2018, pp. 821–867. doi:10.1017/jfm.2018.283.